

Three-dimensional Optical Reconstruction of colloidal electrokinetics via multiplane imaging

Flip de Jong¹, Pablo Diez-Silva², Jui-Kai Chen¹, Raúl Pérez-Peláez², Sudipta Seth¹, Harishankar Balakrishnan³, Bing-Yang Shih⁴, Maarten Rosmeulen⁴, Santi Nonell³, Susana Rocha¹, Andrey Klymchenko⁵, Luis Liz-Marzán^{6,7}, Roger Bresolí-Obach³, Manuel I. Marqués⁸, Rafael Delgado Buscalioni^{2,}, Johan Hofkens^{1,*}, Boris Louis^{1,*}*

¹KU Leuven, Department of Chemistry, Molecular Imaging and Photonics, B-3001 Leuven, Belgium

²Department of Theoretical Condensed Matter Physics, Universidad Autónoma de Madrid, and Condensed Matter Physics Institute (IFIMAC), Campus de Cantoblanco, Madrid 28049, Spain

³Department of Analytical and Applied Chemistry, AppLightChem, Institut Quimic de Sarria, Universitat Ramon Lull, Via Augusta 390, 08007 Barcelona, Catalunya, Spain

⁴imec, Kapeldreef 75, B-3001 Leuven, Belgium

⁵Laboratoire de Bioimagerie et Pathologies, UMR 7021 CRS, Université de Strasbourg, 74 Route du Rhin, Illkirch, 67401, France

⁶CIC biomaGUNE, Basque Research and Technology Alliance (BRTA), 20014 Donostia-San Sebastián, Spain

⁷Centro de Investigación Biomédica en Red, Bioingeniería. Biomateriales y Nanomedicina (CIBER-BBN), 20014 Donostia-San Sebastián, Spain

⁸Departamento de Física de Materiales & Condensed Matter Physics Center (IFIMAC) & Nicolás Cabrera Institute, Universidad Autónoma de Madrid, C. Francisco Tomás y Valiente, 7, 28049 Madrid, Spain.

KEYWORDS Dielectrophoresis, nanomanipulation, 3D imaging, Optical microscopy, Multiplane microscopy

Corresponding Author

* boris.louis@kuleuven.be, johan.hofkens@kuleuven.be, rafael.delgado@uam.es

Abstract

Selective manipulation of particles is crucial in many fields, ranging from chemistry to biology and physics. Dielectrophoresis stands out due to its high selectivity potential and the absence of need for labels. To fully understand and control the phenomenon, observation of the dynamic of nanoparticles under DEP needs to be performed in the three spatial dimensions. However, not many microscopy approaches offer such capability at fast frame rates (>100fps) and high resolution. Here, we used widefield microscopy, to follow the spatiotemporal dynamics of fluorescently labelled polystyrene nanoparticles of 200 nm under positive and negative dielectrophoresis conditions. This real-time 3D imaging technique allows for single particle tracking, enabling super-resolved reconstruction of the DEP force and electrokinetic flows with unprecedented detail. We compare the differences for positive and negative dielectrophoresis conditions and rationalize these by direct comparison with dynamic modeling results. The framework shown here shows great promise to elucidate the frequency-dependent DEP behavior of nanoparticle, crucial for particle manipulation and sorting.

Introduction

Selective manipulation of particles is essential in fields such as chemical and biological analysis, food processing, environmental assessment, diagnostics and cell assays.¹ For example, in biomedicine, sorting distinguishes healthy from diseased cells², while in materials science, precise particle arrangement determines properties like those in photonic crystals or metamaterials.³ This manipulation depends on the particles' physical properties (e.g., size, shape, charge), chemical properties (e.g., material behavior, polarity, solvent/suspension medium), and external force fields (e.g., optical, magnetic, electric)⁴. Among the techniques used to manipulate small particles, dielectrophoresis (DEP) stands out for its rapid, label-free, and highly selective abilities⁵.

DEP refers to the translation of a polarizable particle in a non-uniform electric field. Particles become polarized under an external field, with an induced dipole moment proportional to the field itself. The DEP force arises from the product of two oscillating quantities (dipole times field gradient) whose average is non-zero under alternating (AC) fields. Adjusting the DEP force enables trapping, aligning, isolating, and overall manipulation of particles⁶. The direction of the DEP force is determined by the net polarizability, which for relatively large particles (> 100 nm) can be determined by the Clausius-Mossotti factor (CM)⁷, which depends on the ion conductivity and the dielectric contrast, i.e. the difference between the electric permittivity of the particle (ϵ_p) and the medium (ϵ_m). If the permittivity of the particle at a certain frequency of the oscillating electric field is greater than that of the medium ($\epsilon_p > \epsilon_m$) and the conductivity of particle is lower ($\sigma_p < \sigma_m$), the particle experiences what is called positive DEP (pDEP), and moves moving toward the strong electric field region. Conversely, if the particle's permittivity is lower ($\epsilon_p < \epsilon_m$) and its conductivity higher ($\sigma_p > \sigma_m$) than the medium, it experiences negative DEP (nDEP) and is repelled towards regions of lower field strength^{5,8}. For most dielectric particles, pDEP is found to occur below a crossover frequency (in the order of 0.1 MHz) at which the real part of the polarizability (and thus the DEP force) vanishes. In this standard scenario, nDEP is dominant at higher frequencies. The magnitude of the DEP force usually scales with the particle volume, the gradient of the electric field, and the dielectric contrast between the particle and its surroundings.

Several studies have used DEP to investigate biological elements like DNA⁸, cells⁹, bacteria¹⁰, viruses^{11,12}, and nanostructures like isotropic nanoparticles^{5,11,13}, nanotubes¹⁴, and nanowires¹⁵. Despite its successful application in these areas, the behavior of particles in solutions under alternating electric fields remains an open problem. Theoretical and simulation models including DEP forces and the effect of electrokinetic flow, can predict particle dynamics in certain parameter

range (usually large micron size particles), but this problem is severely multiscale (in time and space) and direct visualization of the particles' movement in three-dimensions (3D) and over time is essential for to advance our understanding of nanoparticle DEP and for direct theoretical validation.⁶

Three-dimensional imaging combined with single particle tracking (SPT) is a promising approach for this task¹⁶. Indeed, it enables the observation of in-plane and out-of-plane motion, which is critical for studying DEP-induced trapping, levitation, and sorting. Furthermore, detailed particle tracking yields real-time trajectories and velocities, allowing calculation of forces acting on individual particles. Although previous attempts using interdigitated transducer electrodes¹⁷, confocal microscopy¹⁸ or digital holography¹⁹ have given some initial hints, these methods have not yet delivered the consistent, high spatial resolution tracking required for reconstructing the motion and force maps. PSF engineering could be a great approach as it allows imaging over large volumes with little to no compromise on the detected photons.^{20,21} However, it suffers from being only applicable to limited concentrations of particles due to the errors that overlapping PSF induces. This is particularly problematic when trying to visualize the capture of a large number of particles on electrodes using DEP. Multiplane microscopy (MPM) is a great solution for this problem because it allows to image a large volume in real-time without strict constraints on- the particle concentration.

Here, we demonstrate the use of custom-designed multi-plane widefield microscopy (MPM),²²⁻²⁴ to track the 3D motion of nanoparticles in the presence of DEP forces generated by AC electric fields. MPM simultaneously records 8 images at different z-depths covering a volume of 40x60x4 mm, enabling real-time, true 3D imaging. We use these techniques to track 200 nm polystyrene (PS) nanoparticles⁵ in 3D and map the AC electric field-induced DEP and flow around a

quadrupolar electrode (commonly encountered in literature). We focus on two conditions: a condition for positive and negative DEP. We show visualization of particles trapped in the space between the electrodes, on top of the electrodes and moving towards or away from the device. Indeed, this deep field of view allows us to unravel the rather complex surface kinetics and 3D dynamics. These experiments provide an unprecedented level of detail in the field of electrokinetics and are combined with dynamical simulation of DEP energy and electrokinetic flows. The framework presented allowing to map DEP and electrokinetic flows and subsequent theoretical analysis is applicable to any electrode geometry and therefore will have a huge impact in particle manipulation and sorting in disciplines such as physics, chemistry, microelectronics, biology and medicine.

Results

Multiplane microscopy and dielectrophoresis setup

To investigate the nanoparticle motion under DEP, we employed a simple quadrupolar electrode (total size $100 \times 100 \mu\text{m}$, separation between the electrodes 600 nm and the depth of the trench is 50 nm) connected to a PCB board and driven by a Keysight waveform generator (EDU33212A) which was controlled by a homemade LabVIEW program. Details of the setup are provided in SI, and the quadrupole device is schematically depicted in Figure 1 alongside a picture of the chip (1a) and a backscattering image of the quadrupole (1b).

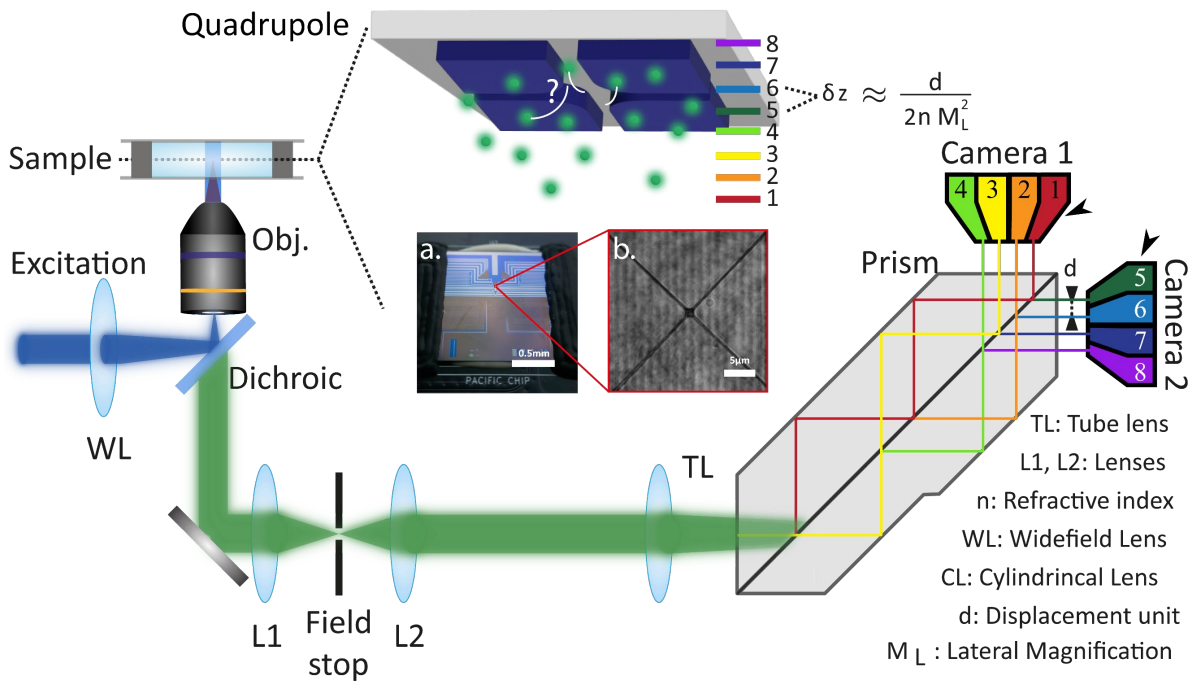


Figure 1: 3D imaging experimental setup: A 488 nm laser is focused on the back aperture of the objective to generate widefield illumination. The light emitted from the sample is collected via an 8f system. A prism beamsplitter split the image in 8, each of the split path having different optical path length which leads to the final image to correspond to a different depth inside the sample. The images are collected 4 by 4 by two synchronized sCMOS. a) Photo of the device containing the quadrupole electrode. b) scattering image of the quadrupole used, representing a very small fraction of the device depicted in a).

For three-dimensional nanoparticle tracking, we used our custom-built multiplane microscope²³, as shown in Figure 1. Briefly, a prism beam splitter divides the detected emission into eight separate images, with 4 collected on each of the two synchronized sCMOS cameras. The prism's geometry creates different optical path lengths between the tube lens and the cameras, conjugating eight distinct z-planes within the sample to 8 different images on the detector. The images are also spatially separated along the x-axis so that four can be recorded on a single detector. The focal plane is positioned such that the top plane is near the electrode interface, enabling imaging of a $50 \times 50 \times 4 \mu\text{m}$ volume at a high frame rate (125 fps). Calibration (see SI) determined an inter-plane distance of approximately 550 nm, with tracking precision 10 nm (x-y) and 20 nm (z) and accuracy of 20 nm (x-y) and 40 nm (z).²³

3D visualization and modelling of 200nm PS particles under positive and negative dielectrophoresis

To visualize the dynamics of 200 nm PS particles under DEP, we first established the voltage and frequency regimes for positive and negative DEP. We then optimized the voltage to ensure that particles moved neither too fast nor too slow, allowing accurate visualization at 125 fps. Two conditions were selected: 100 kHz at 0.5 V to show positive DEP, and 5 MHz at 1 V where the PS particles experience negative DEP. For each condition, at least 10 movies of 10 seconds (1250 frames) were acquired. The particles were subsequently tracked in 3D using our custom algorithm (freely available at <https://github.com/BorisLouis/3D-image-processing>).

Figure 2a and 2d presents the color-coded traces of particle trajectories for positive and negative DEP, respectively; with blue representing the earlier part of the trace and yellow the later part. To avoid crowding the image, only an arbitrary subset (10–50%) of all analyzed traces is shown. Figure 2b and 2e presents the Localization density at the electrode for positive and negative DEP. Figure 2c and 2f show the theoretical results, indicating the DEP energy field and the sketch of the predicted electrokinetic flow.

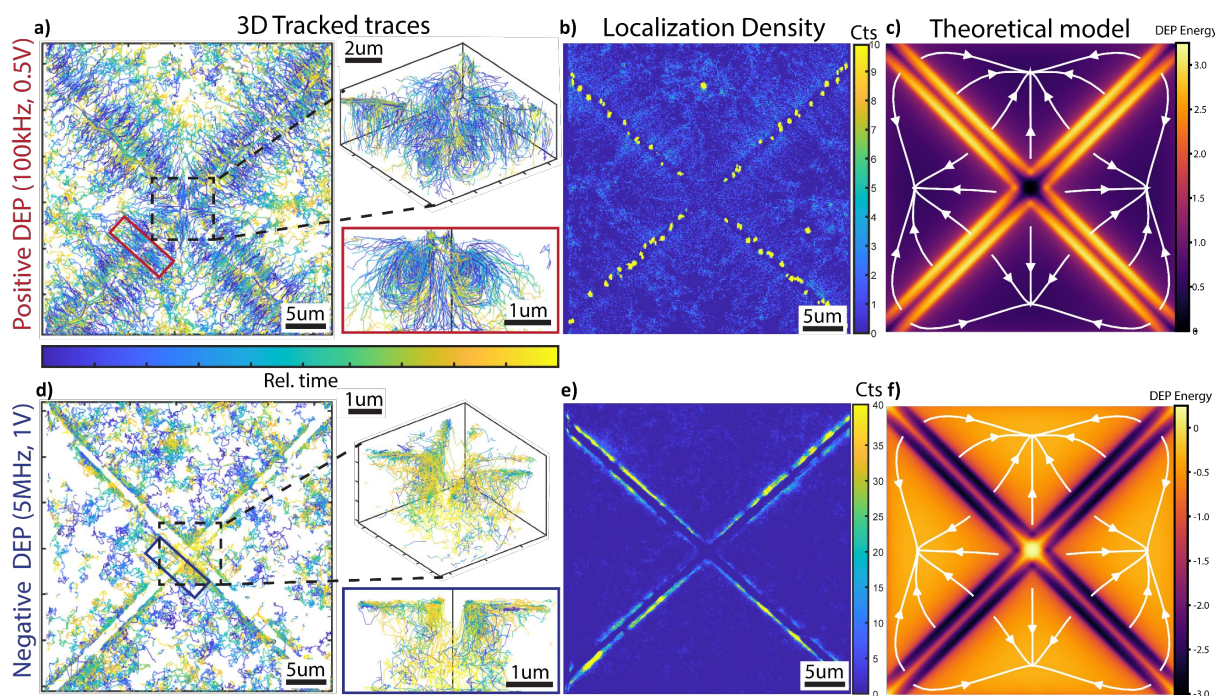


Figure 2: 3D visualization of Positive and negative DEP on 200 nm fluorescent tracers: a) 3D traces combining data from multiple period of 10 second exposition to 100kHz at 0.5V (positive DEP) b) Localization density at the electrode for the same condition c) Theoretical calculation of DEP, the color scale shows the DEP energy, the color scale was adapted to represent positive DEP response while the arrow presents the electrokinetic flows d) 3D traces combining data from multiple period of 10 second exposition to 5MHz at 1V, under negative DEP e) Localization density at the electrode for the same condition f) Theoretical calculations of DEP where the color scale has been adapted to represent a negative DEP response

Figure 2a illustrates the positive DEP condition (100 kHz, 0.5 V) from three perspectives: top view, 3D view, and side view (across an electrode gap). In the top view, regions far from the electrode cross exhibit predominantly Brownian motion, whereas areas near the cross show more directed movement. The high concentration of yellow traces in the gap between the electrodes

confirms particle capture in the region of high electric field strength, i.e. in the electrode gaps, as expected from positive DEP on a quadrupolar electrode. Perpendicular to the electrode, particles appear to be ejected, as traces transition from blue near the electrode to yellow further away. Additionally, particles are expelled from the electrode center in four directions at 45° angles of the electrode axes. These two motions correspond well with the theoretical electrokinetic flow shown as white arrow in panel 2c (see also Fig. 5). The 3D view reveals that traces within the electrode gaps are mainly confined along the electrode plane axis (range <300 nm). Particle arrival follows a semi-hyperboloid profile and ejection occurs in a circular, vortex-like manner (Fig. 5). These complex dynamics could not have been observed without the fast 3D imaging method employed.

The localization histogram of the electrode plane (Figure 2b) clearly shows that particles are predominantly attracted to and confined within the gap between electrodes, close to the electrode edges. This is well represented in the theoretical calculations (Figure 2c), however, under the microscope with 200nm particles, we cannot observe the two edges of the electrode as shown in theory, likely due to the resolution limit. Other flow patterns are also observed but are less dominant due to being statistically less represented in the localization density compared to the particle trapped at the electrode due to their dynamic.

Figure 2d displays corresponding views for negative DEP (5 MHz, 1 V). Two notable differences are observed compared to positive DEP: first, no particles are present in the electrode gap leaving an empty space in the top view in the shape of the cross; second, the top view shows less evidence of directed flow. Particles exhibiting Brownian motion away from the electrode are mostly time-colored blue, while those moving along the electrode near the gap are coded yellow, indicating a flow towards the electrode gap, opposite to the positive DEP scenario. Particles near the electrode gaps sit on top of the electrode and tend to move along the edge without a clear preferential

direction, although the yellow traces at the center of the quadrupole suggest that many paths end there. This is consistent with higher DEP energy on the electrode and at the center of the quadrupole show in the theoretical picture in Figure 2f. We note here that the absence of electrokinetic flow indicates that they are significantly weaker at this frequency (5MHz) compared to the frequency used for positive DEP earlier (100kHz). In the 3D view, we see that particles at the center of the quadrupole are eventually pushed downward, away from the electrode surface. Finally, the localization histogram (Figure 2e) on the electrode plane underscores this difference, with particles clearly avoiding the gap between electrodes under negative DEP as predicted from the theoretical calculation in Figure 2f.

Simulations

Modelling the dynamics of an ensemble of polarizable particles under AC fields requires solving several interrelated phenomena. First, the DEP force

$$F_{DEP} = Re[\alpha] \nabla |E|^2,$$

is obtained from the gradient of the squared electric field, with

$$E = -\nabla\phi$$

arising from the gradient of the potential induced by the electrodes (here a quadrupole). Note that the effective DEP (mechanical) potential can be then considered to be $U_{DEP} = -Re[\alpha] E^2$, and this potential is illustrated in Fig. 2c,f (for pDEP, $Re[\alpha]>0$ and for nDEP ($Re[\alpha] <0$)).

We treat the electrostatic potential as a phasor field and use a finite volume scheme (with a rectangular mesh in collocated form) to solve the Poisson equation

$$\nabla^2 \phi = 0$$

within the neutral electrolyte domain (with constant dielectric permittivity) and just adjacent to the charged diffusive layer, where the charge is localized. The trick, nicely explained by A. Ramos et al.²⁵ is to match with the inner solution (within the charged layer) using appropriate boundary conditions for ϕ , which do resemble those of a perfect capacitor (here we assume the ideal Debye-Hückel scenario). Following²⁵ we impose mixed boundary conditions at (or more appropriate, close to) the electrode plane ($z \sim 0$): in particular

$$\partial_n \phi = A (\phi - V_e)$$

where A is a frequency-dependent constant and V_e is the amplitude of the electrode potential oscillation. Far away from the electrode plane ($z=L$) we use Neumann BC for the potential, corresponding to a negligible electric field. The electrostatic potential also determines the electrokinetic flow created by localized ion currents within the diffusive Debye layer adjacent to the electrodes. The smallness of the diffusive layer (about ten nanometers) allows treating these currents as a slip boundary condition “at” the electrode plane. The slip velocity is given by

$$v_s = B \partial_s \phi,$$

with B a (frequency-dependent) constant and proportional to the gradient at the plane (coordinate s). The slip flow field is indicated in Figure 4. The slip velocity propagates momentum downwards to the fluid and creates the so-called electrokinetic flow, which for the quadrupole setup, is formed by two pairs of counter-rotating vortices (Figure 5). Here we used a new method to calculate the 3D electrokinetic flow from the slip velocity. We placed a rectangular array of N point forces at the surface and used the libMobility tool developed by some of us

[<https://github.com/stochasticHydroTools/libMobility>] to propagate these forces to the bulk, using hydrodynamic Green tensors. We use the slip-mobility tensor (Rotne-Prager-Yamakawa) for the slip-flow domains (electrodes) and the no-slip mobility tensor (Blake) for the no-slip regions (outer domains surrounding the electrodes). The slip velocity field is calculated from the surface electric field, and it determines the point forces located at the surface by an inverse problem, which require the Generalized Minimal Residual Method (GMRES)²⁶ The performance of this route is optimal and faster than solving the fluid dynamic equations in a 3D rectangular grid. Once these point forces are obtained, the electrokinetic flow at any is simply calculated by propagating the point forces to the bulk using the same Green functions. We then solved the nanoparticles dynamics. Inertia is not relevant, and their displacements can be described using Brownian dynamics,

$$dR = (v_{EK} + M F_{DEP}) dt + \sqrt{2kT M} dW$$

dR reflects the displacements of all particles (supervector notation), including the electrokinetic flow at the particle location. In Eq. 1, v_{EK} is the electrokinetic flow, M is the mobility matrix (embedding the hydrodynamic interaction between particles) and kT the thermal energy. The fluctuation-dissipation theorem dictates the diffusion matrix

$$D = kT M$$

whose square root yields the amplitude of the random (thermal) jump, modelled by the vector of independent Wiener increments dW . For details we refer to Refs.^{27,28} In the dilute limit M is diagonal and given by the inverse of the self-particle friction coefficient. Importantly, the 3D time-resolved particle tracking allows us to obtain this field from experiments, which can be directly compared with theory and simulations. For simplicity, in this preliminary work we neglect hydrodynamic interactions (diagonal M).

Mapping forces, flow and directionality in 3D

Using the fast 3D imaging afforded by MPM, we could directly observe how particles move in different conditions around a quadrupolar electrode. Combined with the modelling approach put forward in the previous section, this experimental information can provide a quantitative measure on the DEP force field and accompanying electrokinetic flows. One of the advantages of particle tracking is that it allows to measure the “instantaneous” particle velocity (more precisely $v_p = \frac{\Delta R}{\Delta t}$, with $\Delta t = \frac{1}{125}s$ as the experimental frame sampling frequency). To provide results in units of forces, we derive an effective “electro-kinetic” force which is the sum of the electrokinetic flow “drag” and the DEP force. Multiplying Eq. 1 by the self-friction coefficient $\xi = 6\pi\eta R$, and neglecting hydrodynamic interactions, we get,

$$F_p \equiv \xi v_p = \xi v_{EK} + F_{DEP} \quad (\text{Eq. 2})$$

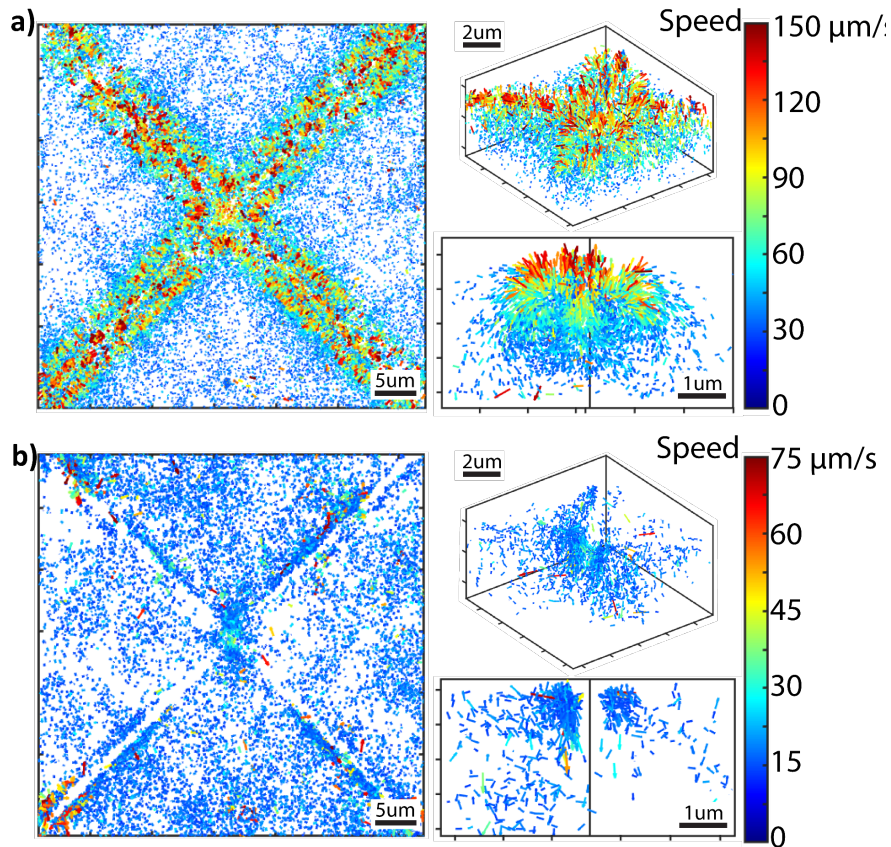


Figure 3: Mapping directed speed in 3D a) Speed vectors for the different field of views presented in Figure 2a. b) Speed vectors for the different field of views presented in Figure 2d

In Figure 3a (positive DEP) the force profile provides a much clearer view of what is happening as we mostly have clear directed force in the regions close to the electrode gap. Speeds are comprised in the range of 0-250 $\mu\text{m/s}$ with 95th percentile at 63 $\mu\text{m/s}$ and a 99th percentile at 145 $\mu\text{m/s}$. This is because the volume where the electrode is active is relatively small compared to the field of view meaning that most of the tracked particles exhibited Brownian or quasi-Brownian motion (which corresponds to an effective force close to 0). In all regions of the electrode gap, the speed is clearly directed from the solution upward (toward the electrode gap). Note that the force is weaker at the center of the cross compared to the gap between two electrodes, which is due to the larger distance between electrodes at the center and is confirmed by the theoretical calculation shown in Figure 2c. Interestingly, the ejection of particles from the electrode gap outward in a

vortex like motions appears very clear with the force vectors pointing radially outward from the gap.

In Figure 3b, we observe forces close to electrode being significantly smaller than for the conditions where we observed positive DEP. Indeed, forces are comprised in the range of 0-100 $\mu\text{m/s}$ with 95th percentile at 52 $\mu\text{m/s}$ and a 99th percentile at 71 $\mu\text{m/s}$. For the nDEP condition employed, the fastest speeds are located on top of the electrode (instead of at the gaps) at the edges of the cross, as well as close to the end of the field of view and the electrode. We note also faster speeds at the center of the quadrupole where particles are pushed down, away from the electrodes. The 3D view offers similar insights where arrows pointing away from the device seem to be the strongest.

Modelling DEP forces and electrokinetic flows

The combined effect of the electrokinetic flow and DEP forcefield on the particle dynamics depends on the frequency and on the voltage. Figure 4 illustrates the slip velocity field adjacent to the electrodes along with the force field associated with pDEP and nDEP at the same plane. Note

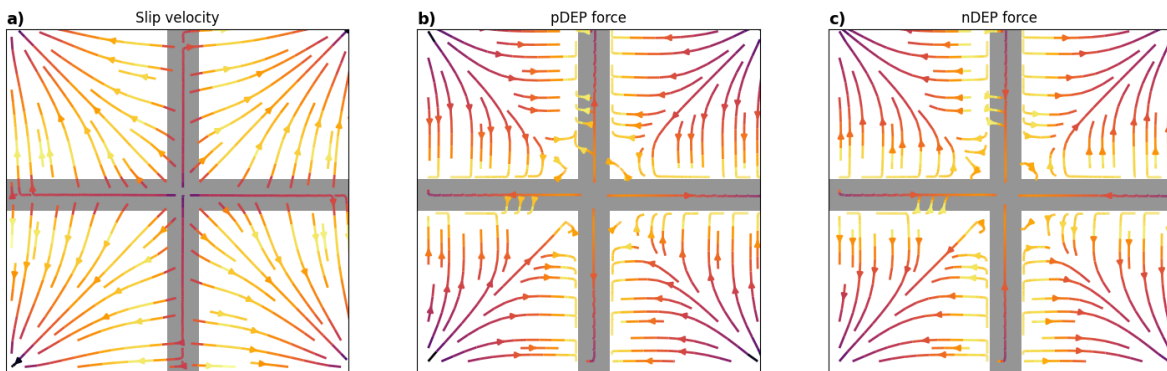


Figure 4: Streamlines of the principal forces acting on a nanoparticle on the electrode. The figure is rotated 45 degrees compared to the experimental setup. The colors represent the force intensity on a logarithmic scale, with yellow indicating stronger forces and purple indicating weaker forces. Units are arbitrary, so the plots are not directly comparable. Electrode gaps are shown in grey. a) Slip velocity streamlines push particles out of the electrode gaps. b) The DEP force under positive DEP (pDEP) conditions pulls particles into the gaps. c) The DEP force under negative DEP (nDEP) conditions pushes particles out of the gaps or toward the center of the electrode.

that the slip velocity field has a similar trend to the nDEP force field as it tends to carry the particles away from the electrodes. However, the resulting 3D flow is highly non-trivial as it also involves the particle diffusion, providing a flux proportional to the gradient of the particle density (and thus to the DEP energy and to EK drift, as established by the Smoluchovski equation). The EK flow is dominant away from the electrodes (in the bulk), as predicted by Ramos et al.²⁵ The 3D structure of the EK flow is illustrated in 5, where theory for the flow streamlines is compared with experimental traces. The portrayed case corresponds to pDEP under a relatively high voltage, as this allows a clearer manifestation of the EK flow (since diffusion becomes less important relatively). Theoretical and experimental streamlines from the particle's velocity field are in excellent agreement and both show how particles reach the electrodes from below (recall the electrodes are placed upside down in the microscopy experiment, see Fig. 1) and form two pairs

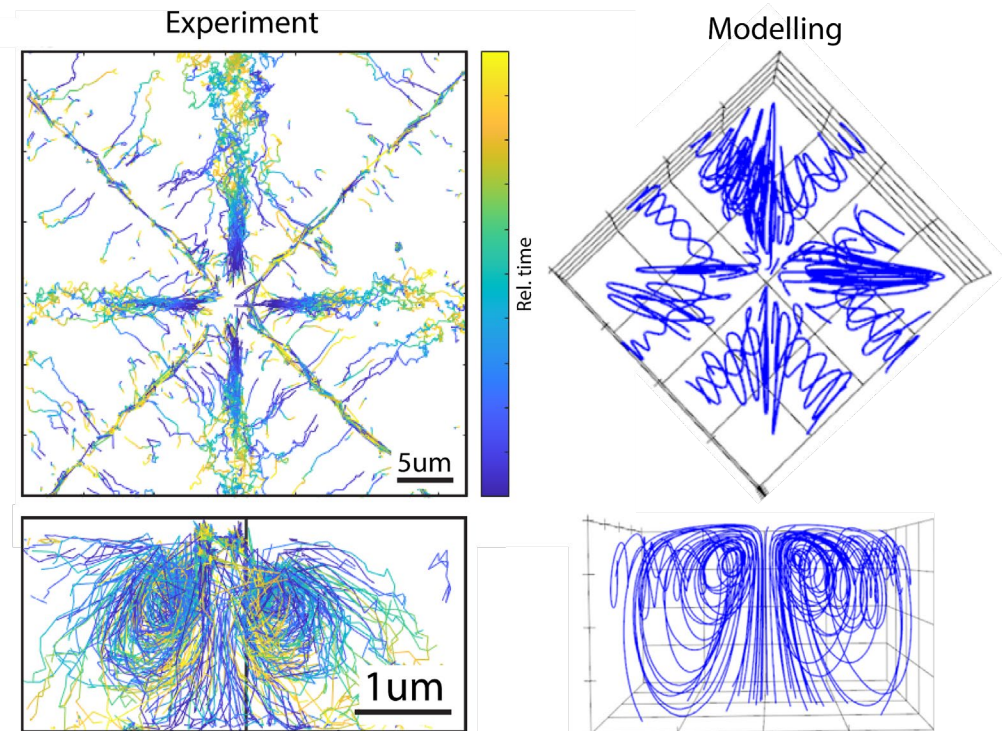


Figure 5: comparison of calculated electrokinetic flows and experimentally observed particle traces. a) Side view of simulation electrokinetic flow. b) Top view of simulation electrokinetic flow. c) Side view of 3D traces ((100 kHz at 0.5 V, pDEP). d) Top view of 3D traces (100 kHz at 0.75 V pDEP).

of counter rotating rolls. A view of the particle traces from below (the xy-plane) clearly shows the bottom-side of these four rolls spreading particles in directions tilted 45 degrees with respect to the quadrupole electrode borders. At this location (away from the electrodes) the particles are expelled out from the center due to the EK hydrodynamic drift. Experiments and simulation results clearly show this effect. In the experimental case, we have also included the particles at the top, attached to the electrode walls, due to DEP forces, and some of their traces perpendicular to the electrode's corridors, due to the slip velocity field.

Conclusions

The data presented in this manuscript represents the first example of 3D mapping of the time-dependent flow of and velocity field of nanoparticles under positive and negative DEP conditions. 3D nanoparticle dynamics on a quadrupolar electrode under AC fields reveal intriguing behaviors under these conditions, particularly when considering the combined effect of electrokinetics and particle diffusion fluxes. Positive DEP attracts particles to the electrode gaps confined along the electrode axis. On the other hand, negative DEP tends to repel particles from the gap between the electrodes by pushing them downward resulting in a complete absence of particles in the electrode gaps. Particles appear, however, attracted to the electrode surface and specifically close to the edge of the electrode. The effect of the EK flow is thus more clearly visible in pDEP, as particles populate the electrode surroundings. The 3D incorporation trajectory driven by ion slip induced EK flows, follows a semi-hyperboloid profile, while the ejection occurs in a circular, vortex-like manner. The prime use of fast 3D multiplane microscopy imaging has enabled detailed visualization and followed by tracking the particle movements, highlighting the complex interplay of DEP forces and electrokinetic flows near a quadrupole electrode. In the future, quantitative analysis of 3D particle speeds combined with a more accurate determination of electrokinetic flows

using theory will reveal the 3D DEP forcefield, leading to a further understanding of the mechanisms driving these dynamics and offering valuable insights for future applications in nanoparticle manipulation and assembly. The direct experimental observation of 3D flow patterns over time shows an unprecedented level of detail that is highly valuable when combined with accurate theory and simulations. It will allow us to measure the particle polarizability under different conditions (notably for small particles) as well as elucidating the details of electrokinetic flow and its interaction with dielectric particles in dense suspensions, where particle-induced EK flows might become relevant, as well as other types of interactions.

Materials and Methods

Multiplane widefield microscope

All experiments have been performed using a multiplane widefield microscope (Figure 1) Briefly, a 488 or 561 nm laser line was used as widefield photoexcitation source by focusing it at the back focal plane of a water-immersion objective lens (N.A.=1.20, 60x, Olympus UplanSApo60XW). The fluorescence emission was collected by the same objective lens and filtered with the suitable optical filter(s) to remove the widefield excitation laser and the emission of the unwanted fluorescent MPs. Afterwards, the emitted light went through a set of lenses in telecentric 4f configuration [Objective - Lens1 – field stop - Lens2 - Tube lens – Camera(s)]. The field stop was used to control the size of the image. Between the tube lens and the cameras, we placed a proprietary prism, which split the entering photon flux into eight different beams with slightly different optical path lengths. The distance between consecutive planes is roughly 580 nm, yielding an axial range of approximately 4 μm . The different imaging planes were recorded by 2 CMOS cameras (4 imaging planes for each camera, Orca Flash 4.0, Hamamatsu Photonics Inc.). To ensure fast acquisition rates (100 fps) and correct synchronization of the two CMOS cameras, we triggered the acquisition via a National Instruments board (NI, USB-6343) coupled to a home-built software written in Labview. The imaging volume was 400 pixels x 400 pixels x 8 planes ($40 \times 40 \times 4 \mu\text{m}^3$).

Single Particle Tracking (SPT) analysis

To track the motion of 200nm diameter PS Fluospheres (Thermofischer, we used a house-written algorithm. The detail of the algorithm used for detecting and tracking the NPs is described elsewhere.²³ Briefly, each NP is detected on different planes and then localized in 3D. After

calculating the (x-, y-, z-) coordinates of each single emitter in the time-lapse image sequence, they were connected in time to form trajectories. The correspondence assignment was performed by minimizing the sum of the displacements of all NPs via Munkres algorithm. Both localization and tracking algorithms are freely available at <https://github.com/BorisLouis/3D-image-processing>.

Sample preparation for microscopy

Since the multiplane widefield microscope (MWM) is an inverted microscope, we used a circular spacer (Grace Bio-Labs SecureSeal™ imaging spacer, diameter 9 mm, thickness 0.12 mm) to create a small sample chamber on the surface of the chip, which holds about 8 μ L of sample solution, and is closed off with a 0.15 mm cover glass. Commercially available fluorescently labelled carboxylate polystyrene (PS) FluoSpheres™ Fluorescent Microspheres (200 nm) s (Invitrogen) were diluted 10mM MES buffer solution (pH=6), enabling control of surface charges and ionic strength. The procedure to prepare the buffer was as follows: 1.952 g MES free acid was dissolved in 800 ml deionized water. 0.442 g KCl was added to fix the ionic strength at 10 mM. Then the final volume of the solution was adjusted to 1000 ml with deionized water. Then the solution was titrated to pH 5.99 with monovalent strong base or acid as needed.

ACKNOWLEDGMENT

This work was funded by the European Union under the Horizon Europe grant 101130615 (FASTCOMET). This work was also supported by the Flemish Government through long term structural funding Methusalem (CASAS2, Meth/15/04), by the Fonds voor Wetenschappelijk Onderzoek-Vlaanderen (FWO, W002221N), by a bilateral agreement between FWO and MOST (VS00721N), by the internal funds of KU Leuven (C14/22/085), by the Spanish Agencia Estatal de Investigación and FEDER (PID2022-137569NA-C44, PID2022-137569NB-C43, PID2020-117080RB-C51 and PDC2021-121441-C21). B.L. acknowledges FWO for his junior postdoctoral fellowship (12AGZ24N). R.B.-O. thanks the Spanish Agencia Estatal de Investigación for a Ramon y Cajal contract (RYC2021-032773-I). MIM acknowledges financial from the Spanish Ministry of Science and Innovation (MCIN), AEI, and FEDER (UE) through Project No.

PID2022-137569NB-C43 and the María de Maeztu Programme for Units of Excellence in R&D (CEX2023-001316-M).

The author thanks Geert Van den Bosch, Senne Fransen, Wim Van Roy, Kruti Trivedi, Radin Tahvildari and Maarten Rosmeulen, for the fabrication of the electrodes, discussions and support in the framework of the FASTCOMET project.

ABBREVIATIONS

DEP dielectrophoresis; pDEP positive dielectrophoresis; nDEP negative dielectrophoresis; EK electrokinetics; MPM multiplane widefield microscopy;

REFERENCES

- (1) Sajeesh, P.; Sen, A. K. Particle Separation and Sorting in Microfluidic Devices: A Review. *Microfluid Nanofluid* **2014**, *17* (1), 1–52. <https://doi.org/10.1007/s10404-013-1291-9>.
- (2) Fontana, F.; Carollo, E.; Melling, G. E.; Carter, D. R. F. Extracellular Vesicles: Emerging Modulators of Cancer Drug Resistance. *Cancers* **2021**, *13* (4), 749. <https://doi.org/10.3390/cancers13040749>.
- (3) John, S. Strong Localization of Photons in Certain Disordered Dielectric Superlattices. *Phys. Rev. Lett.* **1987**, *58* (23), 2486–2489. <https://doi.org/10.1103/PhysRevLett.58.2486>.
- (4) Zhang, S.; Wang, Y.; Onck, P.; Den Toonder, J. A Concise Review of Microfluidic Particle Manipulation Methods. *Microfluid Nanofluid* **2020**, *24* (4), 24. <https://doi.org/10.1007/s10404-020-2328-5>.
- (5) Chen, Q.; Yuan, Y. J. A Review of Polystyrene Bead Manipulation by Dielectrophoresis. *RSC Adv.* **2019**, *9* (9), 4963–4981. <https://doi.org/10.1039/C8RA09017C>.
- (6) Sarno, B.; Heineck, D.; Heller, M. J.; Ibsen, S. D. Dielectrophoresis: Developments and Applications from 2010 to 2020. *Electrophoresis* **2021**, *42* (5), 539–564. <https://doi.org/10.1002/elps.202000156>.
- (7) Hannay, J. H. The Clausius-Mossotti Equation: An Alternative Derivation. *Eur. J. Phys.* **1983**, *4* (3), 141–143. <https://doi.org/10.1088/0143-0807/4/3/003>.
- (8) Regtmeier, J.; Duong, T. T.; Eichhorn, R.; Anselmetti, D.; Ros, A. Dielectrophoretic Manipulation of DNA: Separation and Polarizability. *Anal. Chem.* **2007**, *79* (10), 3925–3932. <https://doi.org/10.1021/ac062431r>.
- (9) Farasat, M.; Aalaei, E.; Kheirati Ronizi, S.; Bakhshi, A.; Mirhosseini, S.; Zhang, J.; Nguyen, N.-T.; Kashaninejad, N. Signal-Based Methods in Dielectrophoresis for Cell and Particle Separation. *Biosensors* **2022**, *12* (7), 510. <https://doi.org/10.3390/bios12070510>.
- (10) Yang, L. A Review of Multifunctions of Dielectrophoresis in Biosensors and Biochips for Bacteria Detection. *Analytical Letters* **2012**, *45* (2–3), 187–201. <https://doi.org/10.1080/00032719.2011.633182>.
- (11) Lapizco-Encinas, B. H.; Rito-Palomares, M. Dielectrophoresis for the Manipulation of Nanobioparticles. *Electrophoresis* **2007**, *28* (24), 4521–4538. <https://doi.org/10.1002/elps.200700303>.
- (12) Nakano, M.; Ding, Z.; Suehiro, J. Dielectrophoresis and Dielectrophoretic Impedance Detection of Adenovirus and Rotavirus. *Jpn. J. Appl. Phys.* **2016**, *55* (1), 017001. <https://doi.org/10.7567/JJAP.55.017001>.
- (13) Gierhart, B. C.; Howitt, D. G.; Chen, S. J.; Smith, R. L.; Collins, S. D. Frequency Dependence of Gold Nanoparticle Superassembly by Dielectrophoresis. *Langmuir* **2007**, *23* (24), 12450–12456. <https://doi.org/10.1021/la701472y>.
- (14) Duchamp, M.; Lee, K.; Dwir, B.; Seo, J. W.; Kapon, E.; Forró, L.; Magrez, A. Controlled Positioning of Carbon Nanotubes by Dielectrophoresis: Insights into the Solvent and Substrate Role. *ACS Nano* **2010**, *4* (1), 279–284. <https://doi.org/10.1021/nn901559q>.
- (15) Kim, D.-J.; Hyung, J.-H.; Seo, D.-W.; Suh, D.-I.; Lee, S.-K. Dual-Gate Multiple-Channel ZnO Nanowire Transistors. *Journal of Elec Materi* **2010**, *39* (5), 563–567. <https://doi.org/10.1007/s11664-009-0984-z>.
- (16) Crocker, J. C.; Grier, D. G. Methods of Digital Video Microscopy for Colloidal Studies. *Journal of Colloid and Interface Science* **1996**, *179* (1), 298–310. <https://doi.org/10.1006/jcis.1996.0217>.

- (17) Alnaimat, F.; Ramesh, S.; Alazzam, A.; Hilal-Alnaqbi, A.; Waheed, W.; Mathew, B. Dielectrophoresis-based 3D-focusing of Microscale Entities in Microfluidic Devices. *Cytometry Pt A* **2018**, *93* (8), 811–821. <https://doi.org/10.1002/cyto.a.23569>.
- (18) Challier, L.; Lemarchand, J.; Deanno, C.; Jauzein, C.; Mattana, G.; Mériquet, G.; Rotenberg, B.; Noël, V. Printed Dielectrophoretic Electrode-Based Continuous Flow Microfluidic Systems for Particles 3D-Trapping. *Part & Part Syst Charact* **2021**, *38* (2), 2000235. <https://doi.org/10.1002/ppsc.202000235>.
- (19) Haapalainen, M.; Kaikkonen, V.; Mäkynen, A. In-Depth Imaging of Dielectrophoresis by Digital in-Line Holographic Microscopy. *Procedia Engineering* **2010**, *5*, 1336–1339. <https://doi.org/10.1016/j.proeng.2010.09.361>.
- (20) Badieirostami, M.; Lew, M. D.; Thompson, M. A.; Moerner, W. E. Three-Dimensional Localization Precision of the Double-Helix Point Spread Function versus Astigmatism and Biplane. *Appl. Phys. Lett.* **2010**, *97* (16), 161103. <https://doi.org/10.1063/1.3499652>.
- (21) Shechtman, Y.; Weiss, L. E.; Backer, A. S.; Sahl, S. J.; Moerner, W. E. Precise Three-Dimensional Scan-Free Multiple-Particle Tracking over Large Axial Ranges with Tetrapod Point Spread Functions. *Nano Lett.* **2015**, *15* (6), 4194–4199. <https://doi.org/10.1021/acs.nanolett.5b01396>.
- (22) Geissbuehler, S.; Sharipov, A.; Godinat, A.; Bocchio, N. L.; Sandoz, P. A.; Huss, A.; Jensen, N. A.; Jakobs, S.; Enderlein, J.; Gisou van der Goot, F.; Dubikovskaya, E. A.; Lasser, T.; Leutenegger, M. Live-Cell Multiplane Three-Dimensional Super-Resolution Optical Fluctuation Imaging. *Nat. Commun.* **2014**, *5*, 5830. <https://doi.org/10.1038/ncomms6830>.
- (23) Louis, B.; Camacho, R.; Bresolí-Obach, R.; Abakumov, S.; Vandaele, J.; Kudo, T.; Masuhara, H.; Scheblykin, I. G.; Hofkens, J.; Rocha, S. Fast-Tracking of Single Emitters in Large Volumes with Nanometer Precision. *Optics Express* **2020**, *28* (19), 28656–28656. <https://doi.org/10.1364/oe.401557>.
- (24) Louis, B.; Huang, C.-H.; Camacho, R.; Scheblykin, I. G.; Sugiyama, T.; Kudo, T.; Melendez, M.; Delgado-Buscalioni, R.; Masuhara, H.; Hofkens, J.; Bresoli-Obach, R. Unravelling 3D Dynamics and Hydrodynamics during Incorporation of Dielectric Particles to an Optical Trapping Site. *ACS Nano* **2023**, *17* (4), 3797–3808. <https://doi.org/10.1021/acsnano.2c11753>.
- (25) Green, N. G.; Ramos, A.; González, A.; Morgan, H.; Castellanos, A. Fluid Flow Induced by Nonuniform Ac Electric Fields in Electrolytes on Microelectrodes. III. Observation of Streamlines and Numerical Simulation. *Phys. Rev. E* **2002**, *66* (2), 026305. <https://doi.org/10.1103/PhysRevE.66.026305>.
- (26) Saad, Y.; Schultz, M. H. GMRES: A Generalized Minimal Residual Algorithm for Solving Nonsymmetric Linear Systems. *SIAM J. Sci. and Stat. Comput.* **1986**, *7* (3), 856–869. <https://doi.org/10.1137/0907058>.
- (27) Peláez, R. P.; Ibáñez-Freire, P.; Palacios-Alonso, P.; Donev, A.; Delgado-Buscalioni, R. Universally Adaptable Multiscale Molecular Dynamics (UAMMD). A Native-GPU Software Ecosystem for Complex Fluids, Soft Matter, and Beyond. *Computer Physics Communications* **2025**, *306*, 109363. <https://doi.org/10.1016/j.cpc.2024.109363>.
- (28) Ermak, D. L.; McCammon, J. A. Brownian Dynamics with Hydrodynamic Interactions. *The Journal of Chemical Physics* **1978**, *69* (4), 1352–1360. <https://doi.org/10.1063/1.436761>.